International Journal of Hydrogen Energy 238 (2026) 155356

Contents lists available at ScienceDirect

International Journal of Hydrogen Energy

journal homepage: www.elsevier.com/locate/he

Metal-coordinated salen-based conjugated microporous polymers derived Ni/N-doped hollow carbon microtubes for enhanced alkaline oxygen evolution electrocatalysis

Yang-Chin Kao [a,1], Mohamed Gamal Mohamed [a,b,*,1], Wei-Hsuan Chang [a], Ahmed F. Saber [c], Shiao-Wei Kuo [a,d,**]

[a] Department of Materials and Optoelectronic Science, Center for Functional Polymers and Supramolecular Materials, National Sun Yat-Sen University, Kaohsiung, 804, Taiwan
[b] Chemistry Department, Faculty of Science, Assiut University, Assiut, 71515, Egypt
[c] Interdisciplinary Research Center for Hydrogen Technologies and Carbon Management (IRC-HTCM), King Fahd University of Petroleum & Minerals, Dhahran, 31261, Saudi Arabia
[d] Department of Medicinal and Applied Chemistry, Kaohsiung Medical University, Kaohsiung, 807, Taiwan

ARTICLE INFO

Keywords:
Oxygen evolution reaction
Thermal transformation
Salen
Conjugated microporous polymers
Hollow carbon microtubes

ABSTRACT

Herein, we report a modular strategy for constructing high-performance OER catalysts via the thermal transformation of metal-linked salen-based conjugated microporous polymers (TPE-SAL-Ni CMP), which was prepared through Sonogashira reaction of 1,1,2,2-tetrakis(4-ethynylphenyl)ethene (TPE-T) with OPDI-Ni-2Br into Ni/N co-doped hollow carbon microtubes. The Ni^{2+} ions coordinated with salen-type ligands (TPE-SAL-Ni CMP) enabled the uniform distribution of the active site. Furthermore, subsequent pyrolysis of TPE-SAL-Ni CMP at 700 °C and 800 °C induced the formation of graphitized carbon frameworks embedded with metallic Ni^0 nanoparticles. TPE-SAL-Ni CMP700 displayed a dramatic reduction in charge-transfer resistance (R_{ct}), an optimized Tafel slope of 93 mV dec^{-1}, and an exceptionally low overpotential of 419 mV at 10 mA cm^{-2}. Structural and spectroscopic analyses revealed the coexistence of Ni^0 and Ni^{2+}–N species, which synergistically enhanced electron transport and reaction kinetics. In addition, TPE-SAL-Ni CMP700 developed a hollow tubular architecture that facilitated electrolyte diffusion and enhanced active site accessibility.

1. Introduction

The oxygen evolution reaction (OER) is central to the operation of various renewable energy devices, including regenerative fuel cells and electrochemical water splitting [1–3]. However, the OER process is inherently sluggish due to its complex four-electron transfer mechanism and multiple adsorbed intermediates, resulting in high overpotentials and poor energy conversion efficiency [4–7]. Currently, state-of-the-art OER catalysts are based on precious metal oxides, such as IrO_2 and RuO_2, which exhibit excellent activity but suffer from high costs, scarcity, and limited durability under alkaline or industrial operating conditions [8,9]. These limitations have driven extensive research toward the development of low-cost, earth-abundant, and efficient electrocatalysts to replace noble metals in practical OER systems. Nickel (Ni), one of the most earth-abundant and cost-effective first-row transition metals, has emerged as a promising candidate for electrocatalytic applications [10–13]. Its versatile redox chemistry (Ni^{2+}/Ni^{3+} and Ni^0/Ni^{2+}), strong affinity for hydroxide ions, and favorable electronic structure make it particularly effective for OER under alkaline conditions [14–25]. However, to fully exploit the catalytic potential of Ni, it is essential to control both its local coordination environment and the electronic conductivity of the host material. To address these design requirements, carbon-based porous materials have been widely utilized as supporting matrices due to their tunable architecture and high

* Corresponding author. Department of Materials and Optoelectronic Science, Center for Functional Polymers and Supramolecular Materials, National Sun Yat-Sen University, Kaohsiung, 804, Taiwan.
** Corresponding author. Department of Materials and Optoelectronic Science, Center for Functional Polymers and Supramolecular Materials, National Sun Yat-Sen University, Kaohsiung, 804, Taiwan.
E-mail addresses: mgamal.eldin12@mail.nsysu.edu.tw (M.G. Mohamed), kuosw@faculty.nsysu.edu.tw (S.-W. Kuo).
[1] These authors contributed equally to this work.

https://doi.org/10.1016/j.ijhydene.2026.155356
Received 22 January 2026; Received in revised form 28 March 2026; Accepted 30 April 2026
Available online 4 May 2026

conductivity after pyrolysis [26–32].

Among these, conjugated microporous polymers (CMPs) stand out as promising precursors for electrocatalysts owing to their rigid π-conjugated backbones, permanent porosity, and high chemical stability [33–40]. CMPs enable precise molecular-level integration of functional groups, facilitating the dispersion of active sites and allowing for heteroatom doping or metal incorporation [41–45]. Upon pyrolysis, CMPs can be converted into nitrogen-doped carbon materials with tailored nanostructures and improved conductivity, making them ideal for electrocatalytic applications [46–48]. In particular, salen-type ligands, which feature N_2O_2 coordination motifs, offer a versatile platform for transition metal binding. Their strong chelating ability ensures uniform metal incorporation [49,50], and their integration into CMPs allows the formation of metal-coordinated porous networks with high nitrogen content and defined coordination geometry. When salen-type ligands coordinate with Ni ions, the resulting salen-based CMPs provide both well-dispersed Ni active sites and nitrogen-rich carbon precursors; upon carbonization at elevated temperatures, these features enable their transformation into highly active Ni/N co-doped electrocatalysts. In our previous work [51], we reported the synthesis of a Ni-coordinated salen-tetraphenylethene (TPE)-based CMP [TPE-SAL-Ni CMP] with a microporous framework and uniformly distributed Ni^{2+} centers. While this material showed enhanced OER activity compared to its metal-free counterpart, its catalytic performance was limited by relatively high overpotential and sluggish kinetics, likely due to insufficient conductivity and partial accessibility of active sites.

In this study, we explored a thermal transformation strategy to enhance the OER performance of TPE-SAL-Ni CMP by directly pyrolyzing it under nitrogen at elevated temperatures (700 °C and 800 °C). The resulting carbonized materials, denoted as TPE-SAL-Ni CMP700 and TPE-SAL-Ni CMP800, undergo significant morphological reorganization, forming hollow carbon microtubes embedded with Ni nanoparticles. This transformation is accompanied by graphitization, which enhances electrical conductivity and facilitates charge transfer. The tubular morphology also provides efficient pathways for electrolyte diffusion and increased exposure of active Ni domains. Among the two samples, TPE-SAL-Ni CMP700 displayed notably improved OER performance, including a substantially reduced overpotential and enhanced kinetic behavior. Electrochemical impedance spectroscopy (EIS) confirmed the reduction in interfacial charge-transfer resistance, while structural analyses revealed that metallic Ni nanoparticles were uniformly embedded within graphitic carbon layers. Spectroscopic characterization further indicated the coexistence of Ni^{2+} and Ni^0 species, implying partial *in-situ* reduction during carbonization. Although nitrogen sorption analysis showed a decrease in surface area, which is commonly observed during pyrolysis due to framework collapse and pore fusion, the enhanced conductivity and activation of Ni domains more than compensated for this structural loss. In summary, this work presents a robust and scalable strategy for fabricating Ni/N co-doped hollow carbon microtubes by pyrolyzing TPE-SAL-Ni CMP. The synergistic combination of conductive carbon architecture, nitrogen-doped frameworks, and uniformly distributed Ni particles leads to superior OER activity in alkaline media. This study not only demonstrates the effectiveness of CMP-based design for advanced electrocatalysts but also highlights the structural tunability and functional versatility of Salen–metal coordination platforms in energy-related applications.

2. Experimental section

2.1. Materials

4-Bromo-2-hydroxybenzaldehyde (99.5%), triphenylphosphine (PPh_3, 99%), N,N-diethylethanamine (Et_3N),tetrakis(triphenylphosphine)-palladium(0) [$Pd(PPh_3)_4$,99%], N,N-dimethylformamide (DMF, 99.9%), copper(I) iodide (CuI, 98%), 1,2-diaminobenzene (1,2-DABZ, 98%) and nickel(II) acetate tetrahydrate [$Ni(CH_3COO)_2{\cdot}4H_2O$, 99%], were obtained from Sigma-Aldrich, Alfa Aesar. Leyan and DUKSAN; respectively. The compound TPE-T was synthesized and fully characterized as reported in our previous study [52–54]. The syntheses of OPDI-2Br [Scheme S1] and OPDI-Ni-2Br [Scheme S2] were also reported in our previous study [51].

2.2. Synthesis of TPE-SAL-Ni CMP

OPDI-Ni-2Br (4 mmol) was coupled with TPE-T (2 mmol) in the presence of CuI (0.4 mmol), PPh_3 (0.4 mmol), and $Pd(PPh_3)_4$ (0.4 mmol) in a binary solvent system of DMF (25 mL) and Et_3N (25 mL). The reaction was vigorously maintained under reflux at 110 °C for 72 h. The crude solid was isolated by filtration and extensively washed with DMF via Soxhlet extraction for three days. Ultimately, TPE-SAL-Ni CMP was obtained as a carrot-colored solid in 57% yield [Scheme 1].

2.3. Carbonization of TPE-SAL-Ni CMP

The as-synthesized TPE-SAL-Ni CMP was subjected to pyrolysis under a nitrogen atmosphere using a single-stage thermal treatment. Approximately 100-200 mg of TPE-SAL-Ni CMP was placed in a ceramic boat and positioned at the center of a tubular furnace. The furnace was purged with high-purity nitrogen (99.999%) at a flow rate of 100 mL min^{-1} for 30 min before heating to ensure an inert environment. The temperature then increased to either 700 °C or 800 °C at a rate of 5 °C min^{-1} and was maintained at the target temperature for 2 h. Then, the furnace was allowed to cool naturally to room temperature under continuous nitrogen flow. The resulting black solid was collected and ground using an agate mortar to obtain a fine powder. The final products were denoted as TPE-SAL-Ni CMP700 and TPE-SAL-Ni CMP800, respectively, according to the pyrolysis temperature [Scheme 1].

3. Results and discussion

3.1. Preparation and structural elucidation of TPE-SAL-Ni CMP and its carbonized forms TPE-SAL-Ni CMP700 and TPE-SAL-Ni CMP800

As depicted in Scheme 1, the Ni^{2+}-coordinated monomer OPDI-Ni-2Br was subjected to a Sonogashira coupling reaction with TPE-T, yielding TPE-SAL-Ni CMP. The resulting TPE-SAL-Ni CMP was subsequently carbonized under a nitrogen atmosphere at 700 °C and 800 °C to afford TPE-SAL-Ni CMP700 and TPE-SAL-Ni CMP800, respectively. TPE-SAL-Ni CMP was characterized by FTIR, solid-state ^{13}C NMR, XRD, XPS, TGA, and Raman spectroscopy to confirm its structure and coordination environment. For the carbonized derivatives [TPE-SAL-Ni CMP700 and TPE-SAL-Ni CMP800], structural and compositional features were investigated using FTIR, XRD, XPS, TGA, and Raman spectroscopy. These characterization techniques collectively provide a comprehensive understanding of the structural evolution from TPE-SAL-Ni CMP to its carbonized forms. To further examine the elemental composition, inductively coupled plasma mass spectrometry (ICP-MS) was performed on all samples. The Ni contents were determined to be 11.8 wt% for TPE-SAL-Ni CMP, 14.5 wt% for TPE-SAL-Ni CMP700, and 14.9 wt% for TPE-SAL-Ni CMP800 [Table S1]. The FTIR spectra of TPE-SAL-Ni CMP, TPE-SAL-Ni CMP700, and TPE-SAL-Ni CMP800 are presented in Fig. 1(a). All three samples exhibit a broad O–H stretching band (3083-3693 cm^{-1}), which remains observable after carbonization, indicating partial retention or reformation of hydroxyl functionalities. A strong band near 1660 cm^{-1} is attributed to C=N and aromatic C=C stretching vibrations, which remain discernible in the carbonized materials, suggesting preservation of the conjugated structure. Notably, the absorption around 1350 cm^{-1}, typically associated with C–N stretching, persists in TPE-SAL-Ni CMP700 and TPE-SAL-Ni CMP800, implying that nitrogen-containing species are at least partially retained during pyrolysis. The retention of nitrogen-containing functionalities is noteworthy, as nitrogen heteroatoms embedded in carbon frameworks have been widely

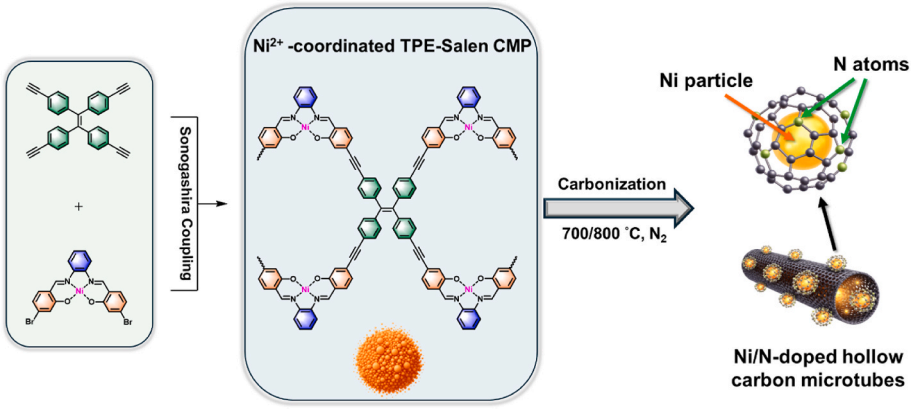

Scheme 1. Schematic illustration of the synthesis of Ni/N-doped hollow carbon microtubes via carbonization of a Ni^{2+}-coordinated salen-based CMP [TPE-SAL-Ni CMP].

reported to enhance electrocatalytic activity toward oxygen evolution reactions (OER) by modulating the electronic structure and generating catalytically active sites. Raman spectra of TPE-SAL-Ni CMP, TPE-SAL-Ni CMP700, and TPE-SAL-Ni CMP800 are shown in Fig. S1. Upon carbonization, two distinct bands emerge near ~1340 cm^{-1} (D band) and ~1580 cm^{-1} (G band), which are characteristic of disordered carbon and graphitic sp^2-hybridized carbon, respectively. These features are absent from the pristine TPE-SAL-Ni CMP, indicating that the conjugated polymer framework undergoes a significant structural transformation upon thermal treatment. In addition, the presence of both D and G bands in TPE-SAL-Ni CMP700 and TPE-SAL-Ni CMP800 confirms the formation of carbonaceous domains during the pyrolysis process. The intensity ratio of the D and G bands (I_D/I_G) is often used as an indicator of defect density and graphitization degree in carbon materials [55–58]. In this case, TPE-SAL-Ni CMP700 exhibits an I_D/I_G value of 0.989, while TPE-SAL-Ni CMP800 displays a slightly higher ratio of 1.008. The marginal increase in I_D/I_G suggests that higher pyrolysis temperature leads to a modest increase in structural disorder, possibly due to the partial degradation of the polymer network or increased formation of edge defects. These results imply that tuning the carbonization temperature can modulate the structural ordering and defect characteristics of the resulting carbon frameworks, which may in turn affect their electrochemical properties. According to the solid-state ^{13}C NMR data of TPE-SAL-Ni CMP, the carbon resonances in the range 100-139 ppm are mainly assigned to aromatic carbon atoms, whereas signals in the 90–100 ppm range are associated with acetylenic carbons [51]. Distinct peaks were detected at 143 ppm, corresponding to the C=C bonds of the TPE moieties, at 156 ppm attributed to aromatic C–OH groups, and at 161 ppm related to the C=N functionality, which are consistent with the expected structure of the Ni-coordinated CMP framework [51]. Notably, the overall signal intensity and signal-to-noise ratio are relatively low, which is attributed to the paramagnetic nature of Ni^{2+} centers. The unpaired electrons of high-spin d^8 Ni^{2+} [Scheme S3] can induce rapid spin relaxation and line broadening, thereby reducing the NMR detectability of nearby nuclei. Fig. 1(b) displays the powder X-ray diffraction (XRD) patterns of TPE-SAL-Ni CMP and its carbonized derivatives. The pristine TPE-SAL-Ni CMP exhibits a broad, featureless profile, characteristic of an amorphous polymer lacking long-range crystallinity. In contrast, TPE-SAL-Ni CMP700 and TPE-SAL-Ni CMP800 show distinct diffraction peaks at $2\theta \approx 44.4°$, 51.7°, and 76.1°, which correspond to the (111), (200), and (220) planes of face-centered cubic (fcc) metallic nickel (JCPDS No. 01-1258) [59–61]. These reflections confirm the *in-situ* formation of crystalline Ni nanoparticles upon pyrolysis under an inert atmosphere. Using the Scherrer equation, the average crystallite sizes of Ni were estimated to be approximately 14.1 nm for TPE-SAL-Ni CMP700 and 16.7 nm for TPE-SAL-Ni CMP800, based on the (111) reflection.

The increase in crystallite size at higher temperature suggests thermally driven grain growth, likely due to enhanced mobility and aggregation of Ni species during carbonization. A weak and broad diffraction feature centered at ~41.8° is also observed in both carbonized samples, assignable to the (100) plane of graphitic carbon. This feature indicates partial in-plane ordering within the carbon matrix, consistent with the structural evolution induced by high-temperature treatment. Overall, XRD analysis demonstrates that thermal carbonization not only generates embedded Ni nanocrystals but also promotes the development of graphitic carbon domains. These observations complement the Raman results and provide structural evidence of the transformation from amorphous TPE-SAL-Ni CMP to a hybrid carbon–metal composite. An in-depth structural analysis of TPE-SAL-Ni CMP and its carbonized derivatives (TPE-SAL-Ni CMP700 and TPE-SAL-Ni CMP800) was conducted using X-ray photoelectron spectroscopy (XPS) to investigate the bonding environments of C, N, O, and Ni centers [Fig. 1(c)]. The high-resolution C 1s spectra [Fig. S2(a)] display three major components. The first peak, located at 283.9-284.3 eV, is attributed to **C**–C, **C**=C, and **C** ≡C bonding environments. The second peak, at 285.0-285.5 eV, is assigned to **C**–N and **C**=N species, indicating nitrogen incorporation into the framework. The third component, observed at 286.1-286.7 eV, corresponds to **C**–O bonds, suggesting the formation of oxygen-containing chemical functionalities. The N 1s spectra [Fig. S2(b)] of the TPE-SAL-Ni CMP sample show two peaks at 398.8 eV and 399.9 eV, attributed to C–N/CN functionalities and Ni–N coordination, respectively. After thermal treatment (TPE-SAL-Ni CMP700 and TPE-SAL-Ni CMP800), the N 1s spectra [Fig. S2(b)] become more complex and can be deconvoluted into multiple nitrogen species. Specifically, several characteristic peaks are identified: a peak at ~398.0-398.2 eV corresponding to pyridinic-N, a peak at ~398.3-399.5 eV assigned to Ni–N coordination, a peak at ~400.0-400.3 eV attributed to pyrrolic-N, a peak at ~400.5-400.7 eV corresponding to graphitic-N, a peak at ~401.6-401.9 eV assigned to quaternary-N, and a high-binding-energy peak at ~403.2-403.7 eV attributed to oxidized-N species. The content of XPS data [Table S2] reveals notable changes in nitrogen speciation with increasing pyrolysis temperature. For TPE-SAL-Ni CMP700, pyridinic-N (33.02%) and pyrrolic-N (31.84%) are the dominant species, followed by graphitic-N (16.42%), quaternary-N (8.26%), Ni–N (5.42%), and oxidized-N (5.04%). In contrast, for TPE-SAL-Ni CMP800, the proportion of graphitic-N significantly increases to 32.66%, becoming the predominant nitrogen species, while pyridinic-N (30.24%) and pyrrolic-N (18.46%) decrease. Meanwhile, Ni–N (6.32%) and oxidized-N (5.29%) show slight increases, whereas quaternary-N decreases to 7.04%. The O 1s spectra [Fig. S2(c)] show a peak at 531.3 eV in TPE-SAL-Ni CMP, assigned to phenolic C–**O** bonds, along with a peak at 532.6 eV, attributed to Ni–O coordination. In TPE-SAL-Ni CMP700 and TPE-SAL-Ni CMP800, two components are observed: one at 531.1 eV,

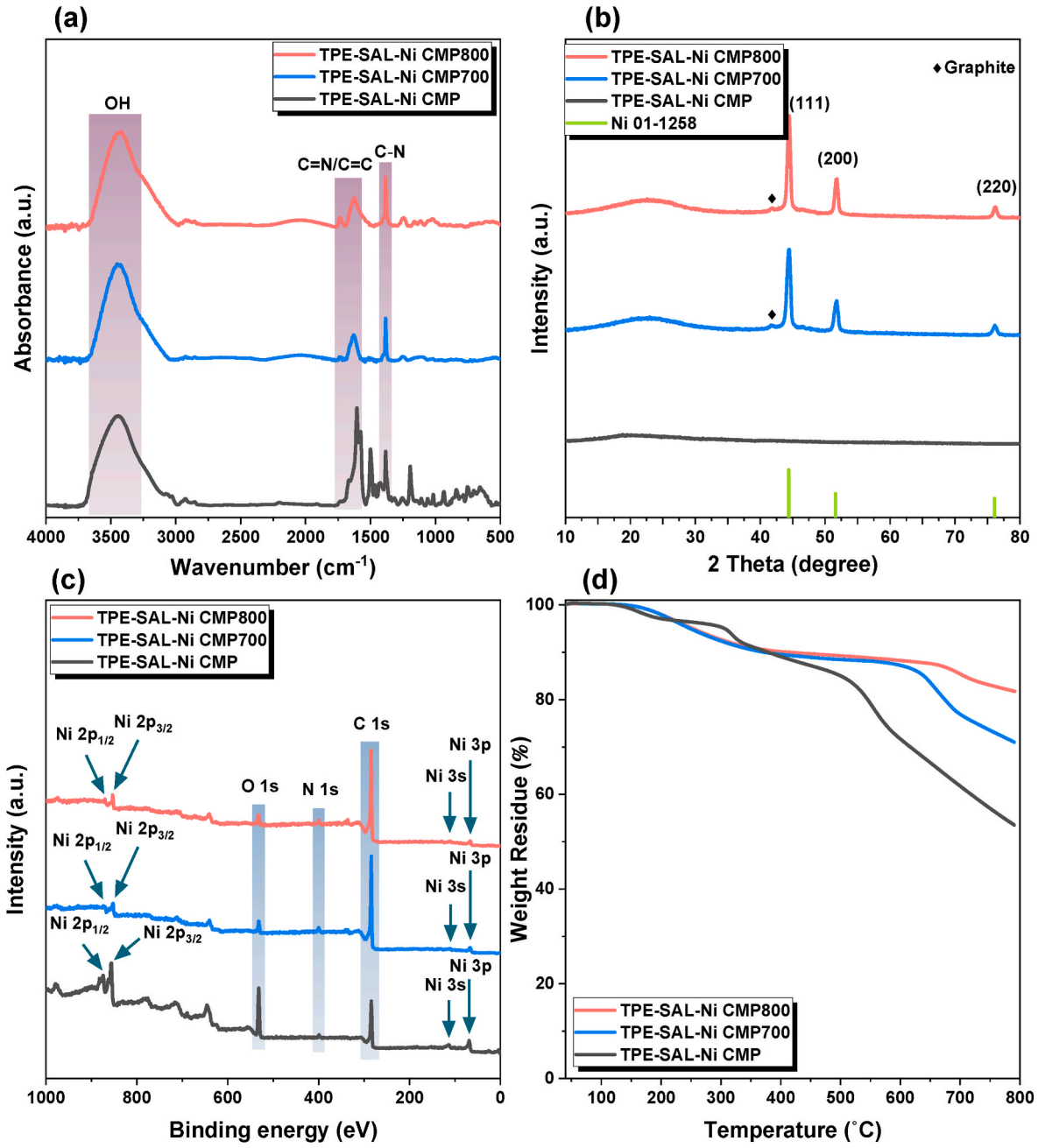

Fig. 1. (a) FTIR spectra, (b) PXRD patterns, (c) wide-scan XPS survey spectra, and (d) TGA curves of TPE-SAL-Ni CMP, TPE-SAL-Ni CMP700, and TPE-SAL-Ni CMP800.

corresponding to C–O, N–O, or N=O groups; and another at 532.3-532.5 eV, attributed to Ni–O coordination. The presence of these components across all samples indicates stable metal–oxygen bonding, while the emergence of additional oxygen-containing species after carbonization suggests structural and chemical evolution of the surface.

In Fig. 2(a), high-resolution Ni 2p XPS spectra were recorded to determine the chemical state of nickel present in the samples. The spectrum of TPE-SAL-Ni CMP reveals two main peaks at approximately 856.5 eV (Ni^{2+} $2p_{3/2}$) and 874.2 eV (Ni^{2+} $2p_{1/2}$) [62,63], along with their associated satellite features, which are characteristic of Ni^{2+} species. Notably, no signal corresponding to metallic nickel is detected in this pristine sample. After pyrolysis, the spectrum undergoes significant evolution. In TPE-SAL-Ni CMP700, the appearance of peaks at 852.3 eV (Ni^0 $2p_{3/2}$) and 869.6 eV (Ni^0 $2p_{1/2}$) indicates the formation of metallic Ni (Ni^0), while the remaining peaks at 855.1 eV (Ni^{2+} $2p_{3/2}$) and 873.1 eV (Ni^{2+} $2p_{1/2}$) confirm the partial retention of Ni^{2+}. Similarly, TPE-SAL-Ni CMP800 exhibits metallic Ni signals at 852.6 eV (Ni^0 $2p_{3/2}$) and 869.9 eV (Ni^0 $2p_{1/2}$), alongside Ni^{2+} peaks at 854.7 eV ($2p_{3/2}$) and 873.6 eV ($2p_{1/2}$) [62,63]. The coexistence of Ni^0 and Ni^{2+} states in the pyrolyzed samples suggests partial in situ reduction of nickel species during thermal treatment. Furthermore, the subtle shift in binding energies and the relative intensities between Ni^0 and Ni^{2+} signals reflect the progressive reduction of Ni with increasing pyrolysis temperature. This dual chemical environment, consisting of both coordinated Ni^{2+} centers and metallic Ni domains, is often associated with enhanced electron transport and catalytic activity in carbon-based materials [23,64]. To assess the thermal stability of the prepared materials, thermogravimetric analysis (TGA) measurements were carried out on TPE-SAL-Ni CMP, TPE-SAL-Ni CMP700, and TPE-SAL-Ni CMP800 under a nitrogen atmosphere, as shown in Fig. 1(d). The temperature at 10%

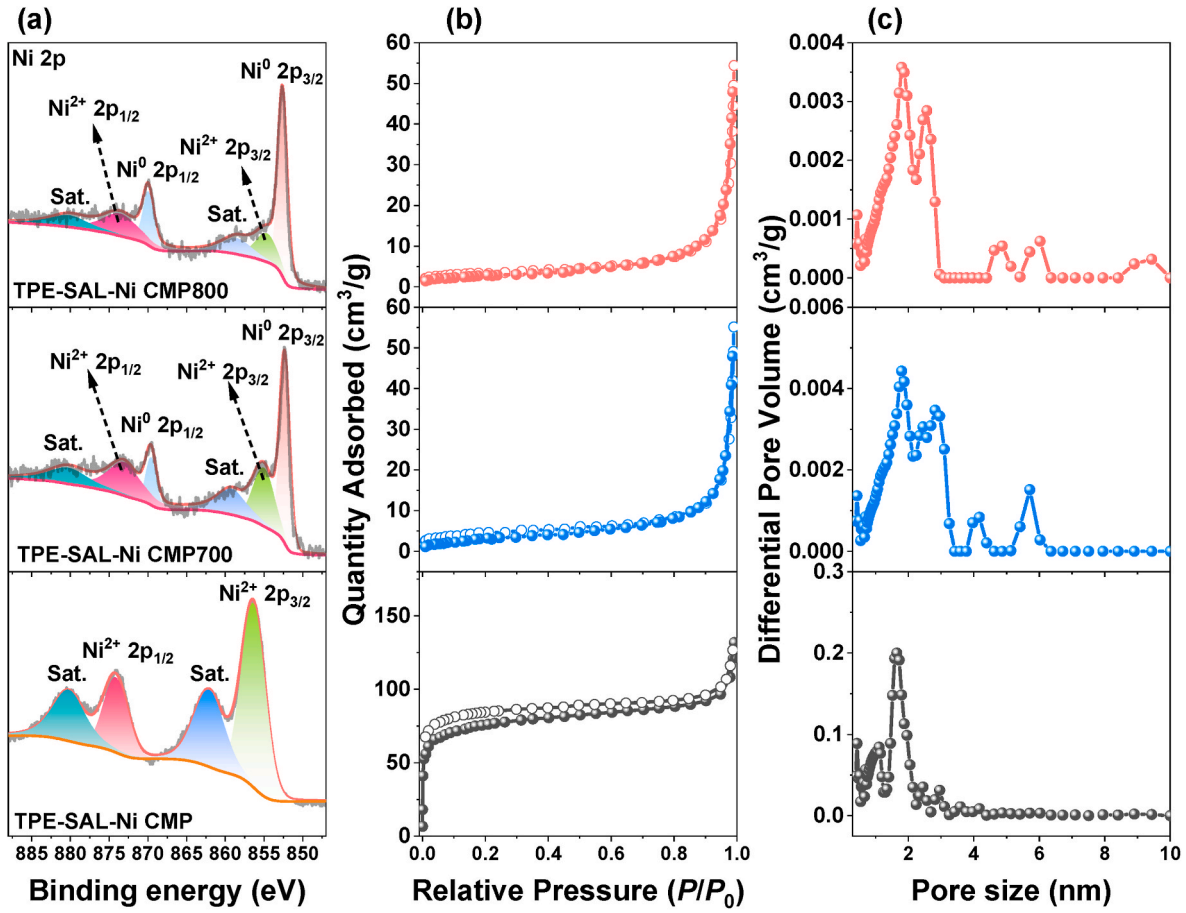

Fig. 2. (a) High-resolution Ni 2p XPS spectra, (b) N_2 adsorption–desorption isotherms measured at 77 K, and (c) pore size distribution curves [determined from the adsorption branch using the NLDFT approach] of TPE-SAL-Ni CMP, TPE-SAL-Ni CMP700, and TPE-SAL-Ni CMP800.

weight loss (T_{d10}) was found to be 379 °C for TPE-SAL-Ni CMP, 373 °C for TPE-SAL-Ni CMP700, and 415 °C for TPE-SAL-Ni CMP800 [Fig. S3]. While TPE-SAL-Ni CMP800 exhibits the highest decomposition temperature and char yield, TPE-SAL-Ni CMP700 achieves a favorable balance between thermal stability and carbon retention. Specifically, TPE-SAL-Ni CMP700 displays a char yield of ~71.1 wt%, significantly higher than that of the pristine TPE-SAL-Ni CMP (~53.5 wt%), indicating improved carbon content and structural robustness after pyrolysis. This intermediate level of graphitization and heteroatom retention is expected to enhance electrical conductivity while maintaining a considerable density of potential active sites. These results indicate that thermal treatment at 700 °C produces a carbon framework with favorable structural characteristics that may be beneficial for electrocatalytic applications. The porosity evolution of TPE-SAL-Ni CMP and its carbonized samples (TPE-SAL-Ni CMP700 and TPE-SAL-Ni CMP800) was evaluated using nitrogen adsorption–desorption isotherm analysis. As shown in Fig. 2(b), the pristine TPE-SAL-Ni CMP exhibited a type IV isotherm with an H3-type hysteresis loop, indicating the presence of mesoporous features associated with the amorphous polymer network. The BET surface area was determined to be 281 $m^2\ g^{-1}$, with a dominant pore size of ~1.7 nm based on NLDFT analysis [Fig. 2(c)]. This pore size falls near the micropore–mesopore boundary, consistent with the typical porosity range of conjugated microporous polymers. Despite its high surface area, TPE-SAL-Ni CMP showed limited catalytic activity, which arises from insufficient electronic conductivity and restricted exposure of catalytically active sites, as revealed by electrochemical analysis. Upon thermal treatment at 700 °C, the surface area of TPE-SAL-Ni CMP700 drastically decreased to 15 $m^2\ g^{-1}$. While the mesoporous character was retained, the total nitrogen uptake significantly declined, and the pore size distribution broadened to a range of 1.8-5.7 nm [Fig. 2 (c)], reflecting partial framework collapse and pore fusion. This reduction in surface area is commonly observed during carbonization and is attributed to the decomposition of organic linkers and structural reorganization. In contrast, TPE-SAL-Ni CMP800 exhibited a further reduction in surface area to 11 $m^2\ g^{-1}$, along with a flattened isotherm profile and diminished hysteresis loop, suggesting less well-defined mesoporous features and possible structural densification. Scanning electron microscopy (SEM) was used to investigate the morphological evolution of TPE-SAL-Ni CMP, TPE-SAL-Ni CMP700, and TPE-SAL-Ni CMP800, as shown in Fig. 3(a) and (b), the pristine TPE-SAL-Ni CMP exhibits dense, irregularly packed microscale aggregates composed of interconnected nanoscale particles with rough surfaces and distinct interparticle voids, indicating the presence of a hierarchical porous structure. After pyrolysis at 700 °C, a dramatic structural transformation is observed [Fig. 3 (c)]. The framework reorganizes into a robust, hollow tubular carbon architecture, uniformly decorated with ultra-fine metallic nanoparticles. These nanoparticles originate from the *in-situ* reduction of Ni^{2+} ions within the CMP network to metallic Ni^0 under an inert atmosphere. The reduced Ni^0 species are believed to catalyze the reorganization of the carbon framework during pyrolysis, leading to a stable rod-like morphology. Upon further pyrolysis at 800 °C [Fig. 3(d)], the tubular frameworks remain intact, while the surface Ni^0 nanoparticles grow slightly larger and appear more uniformly spaced, resulting in a characteristic "pearl-on-string" structure. This difference in particle size and density likely arises from increased atomic mobility at elevated temperatures, resulting in moderate coarsening. This hierarchical tubular architecture, along with the uniform dispersion of Ni^0 nanoparticles, is expected to facilitate electrolyte penetration and maximize the exposure

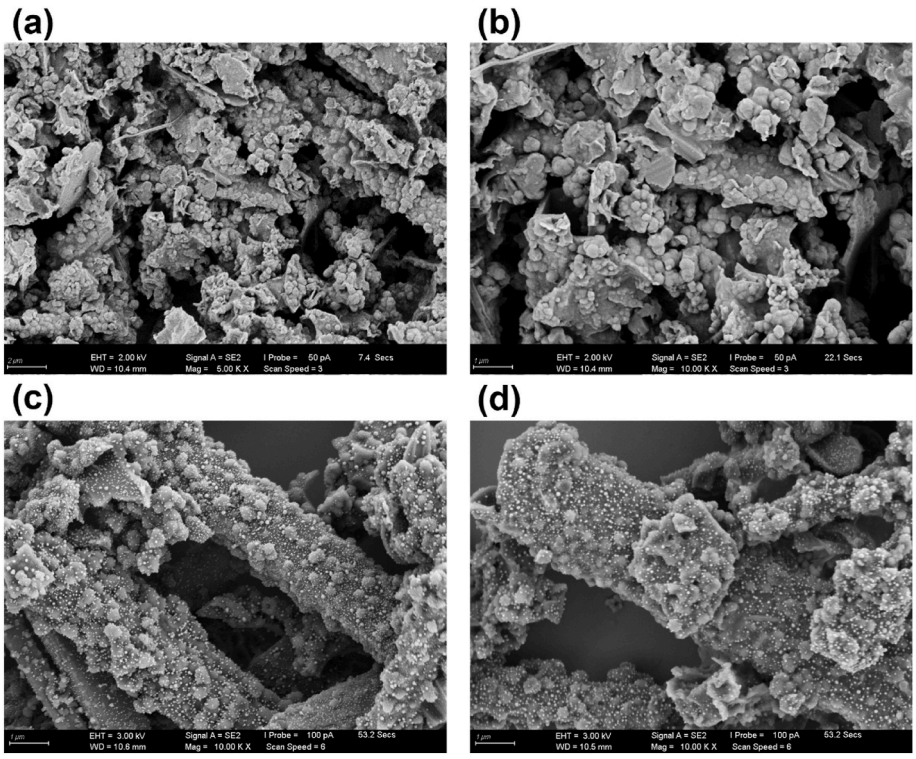

Fig. 3. SEM images of (a, b) TPE-SAL-Ni CMP, (c) TPE-SAL-Ni CMP700 and (d) TPE-SAL-Ni CMP800.

of active Ni sites, which are advantageous for electrocatalytic applications.

Furthermore, TEM analysis furnished additional structural evidence to support the morphological evolution observed in SEM. The bright-field TEM image [Fig. S4] reveals that the pristine TPE-SAL-Ni CMP consists of aggregated polymeric particles without discernible crystalline features, consistent with its amorphous nature. After pyrolysis at 700 °C (TPE-SAL-Ni CMP700), dark nanoparticles begin to appear on the carbon matrix, indicating the formation of metallic Ni domains [Fig. S5]. At 800 °C (TPE-SAL-Ni CMP800), these particles become more prominent and noticeably larger, suggesting thermally induced growth and aggregation of Ni species during carbonization [Fig. S6]. This observation is in agreement with the crystallite sizes estimated from XRD. Further insights into the local structure were obtained from HRTEM and selected area electron diffraction (SAED) analyses of TPE-SAL-Ni CMP700. The HRTEM image [Fig. 4(a)] reveals well-resolved lattice fringes with interplanar spacings of 0.204 nm and 0.336 nm, corresponding to the (111) plane of metallic Ni and the (002) plane of graphitic carbon, respectively. These features confirm the formation of crystalline Ni^0 nanoparticles embedded within a graphitized carbon matrix. The corresponding SAED pattern [Fig. 4(b)] displays concentric diffraction rings that can be indexed to the (111), (200), and (220) planes of face-centered cubic (fcc) Ni, further validating the *in-situ* reduction and crystallization of Ni species during pyrolysis. Additionally, HRTEM images [Fig. 4(c) and (d)] further reveal that these Ni nanoparticles are embedded on the surfaces of hollow carbon tubes, clearly highlighting their intimate interfacial contact with the carbon matrix. Such a configuration is expected to promote efficient electron transport and maximize active site accessibility for electrocatalytic applications. To complement these results, TEM-energy-dispersive X-ray spectroscopy (TEM-EDX) elemental mapping of TPE-SAL-Ni CMP, TPE-SAL-Ni CMP700, and TPE-SAL-Ni CMP800 is provided in Fig. S4–S6. All three samples exhibit a homogeneous distribution of C, N, O, and Ni throughout the framework. In the case of TPE-SAL-Ni CMP800, the EDX mapping also reveals the characteristic tubular morphology, further confirming the formation and retention of hollow carbon structures upon high-temperature pyrolysis. Taken together with XPS and Raman analyses, these TEM results highlight the dual contribution of graphitized carbon frameworks and well-dispersed Ni^0/Ni^{2+} species as key factors for enhanced electrocatalytic performance. The graphitized tubular architecture facilitates efficient electron transport and electrolyte diffusion, while the coexistence of metallic Ni and Ni–N coordination sites provides abundant and accessible active centers. To further substantiate this proposed synergistic effect, density functional theory (DFT) calculations were performed at the B3LYP/6-31G(d) level to elucidate the electronic structures of the Ni^{2+}-coordinated salen-based CMPs and their corresponding monomers [Fig. S7]. For the TPE-SAL-Ni CMP, the highest occupied molecular orbital (HOMO) is predominantly localized on the ligand framework with a minor contribution from the Ni center, whereas the lowest unoccupied molecular orbital (LUMO) is mainly centered on the Ni atom with slight delocalization over the ligand. A similar distribution is observed for the corresponding monomer, OPDI-Ni-2Br, where the HOMO resides primarily on the ligand and the LUMO is largely localized on the Ni center. In contrast, both the HOMO and LUMO of TPE are delocalized over the phenyl and vinylene units. These results demonstrate a complementary electronic interaction between the metal-centered and ligand-based orbitals, which promotes effective charge transfer between the Ni active sites and the conjugated framework. Such electronic coupling, together with the conductive tubular structure, provides theoretical evidence for the synergistic effect, thereby rationalizing the enhanced catalytic performance. Structural characterization by XRD, Raman spectroscopy, and TEM reveals that TPE-SAL-Ni CMP700 develops a hollow tubular carbon framework embedded with metallic Ni nanoparticles and graphitized carbon domains. These features enhance electrical conductivity and facilitate charge and mass transport, thereby offsetting the loss of surface area caused by carbonization. In addition, XPS analysis confirms the coexistence of Ni^0 and Ni^{2+} species, suggesting the presence of dual active sites that are favorable for the OER. By comparison, TPE-SAL-Ni CMP800 shows a further reduction in surface area, along with a flatter nitrogen adsorption–desorption isotherm and a weakened hysteresis loop, indicating less well-defined mesoporosity and a more compact

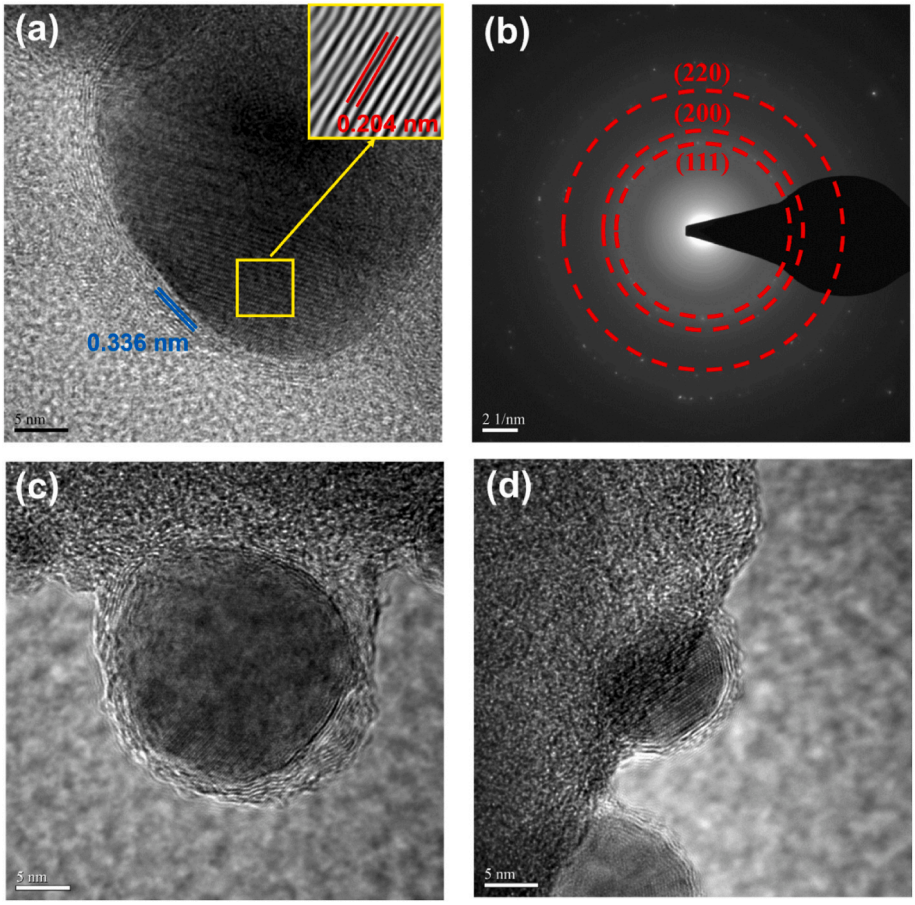

Fig. 4. (a) High-resolution TEM image of TPE-SAL-Ni CMP700 showing well-defined lattice fringes. Inset: inverse Fast Fourier Transform (IFFT) of the Ni lattice. (b) SAED pattern of TPE-SAL-Ni CMP700, confirming the crystalline nature of metallic Ni. (c, d) HRTEM images revealing Ni nanoparticles embedded on the surface of the tubular carbon matrix in TPE-SAL-Ni CMP700.

structure. The larger Ni crystallite size and higher defect density observed in TPE-SAL-Ni CMP800, together with the slightly increased I_D/I_G ratio in the Raman spectra [Fig. S1], suggest that excessive thermal treatment at 800 °C induces structural collapse of the carbon framework and reduces the accessibility of active sites. Therefore, the temperature range of 700 °C and 800 °C was selected to evaluate the effect of carbonization severity, and the results demonstrate that 700 °C provides the optimal balance among porosity, graphitization, and active-site formation. As a result, TPE-SAL-Ni CMP700 exhibits the most favorable structural features for OER catalysis, which is further supported by the electrochemical results presented in the following section.

3.2. Electrocatalytic performance of TPE-SAL-Ni CMP, TPE-SAL-Ni CMP700 and TPE-SAL-Ni CMP800 for oxygen evolution reaction (OER)

OER activity of all synthesized materials was systematically evaluated using a conventional three-electrode system in an aqueous electrolyte (1 M). Linear sweep voltammetry (LSV) was employed to measure the anodic polarization curves [Fig. 5(a)]. Among all samples, TPE-SAL-Ni CMP700 demonstrated the best performance, requiring an overpotential of only 419 mV to reach 10 mA cm^{-2}, which is significantly lower than TPE-SAL-Ni CMP800 (474 mV) and TPE-SAL-Ni CMP (505 mV) [Fig. 5(b)]. To probe the catalytic kinetics, Tafel analysis was conducted by plotting overpotential versus the logarithm of current density [Fig. 5(c)]. TPE-SAL-Ni CMP700 exhibited the lowest Tafel slope of 93 mV dec^{-1}, compared to 117 mV dec^{-1} for TPE-SAL-Ni CMP800 and 182 mV dec^{-1} for TPE-SAL-Ni CMP, signifying a faster electron transfer rate and more favorable reaction pathway for oxygen evolution on TPE-SAL-Ni CMP700 [65,66]. Electrochemical impedance spectroscopy (EIS) was conducted to study the interfacial R_{ct} under OER operating conditions [Fig. 5(e)]. The Nyquist plots reveal that TPE-SAL-Ni CMP700 exhibits the smallest R_{ct} of 86 Ω, followed by TPE-SAL-Ni CMP800 (87 Ω) and TPE-SAL-Ni CMP (298 Ω) [Table S3], confirming that the 700 °C-treated sample possesses enhanced electrical conductivity and a lower energy barrier for interfacial charge transport. To estimate the number of accessible electrochemical active sites, the electrochemical double-layer capacitance (C_{dl}) was calculated from cyclic voltammetry (CV) curves recorded in the non-faradaic potential region at various scan rates [Fig. S8]. The C_{dl} value of TPE-SAL-Ni CMP700 (0.021 mF) is higher than that of TPE-SAL-Ni CMP800 (0.016 mF) and TPE-SAL-Ni CMP (0.015 mF) [Fig. 5(d)], indicating a greater surface area for electrochemical interactions. Based on these values, the electrochemical surface area (ECSA) was estimated to be 0.525 cm^2 for TPE-SAL-Ni CMP700, 0.400 cm^2 for TPE-SAL-Ni CMP800, and 0.375 cm^2 for TPE-SAL-Ni CMP [Fig. S9], further confirming the exposure of more active sites in TPE-SAL-Ni CMP700 due to its optimized nanostructure. The intrinsic catalytic activity was also evaluated via turnover frequency (TOF) measurements at varying overpotentials. As shown in [Fig. S10], TPE-SAL-Ni CMP700 exhibited a steady increase in TOF from 11.1 s^{-1} at 370 mV to 78.9 s^{-1} at 470 mV, demonstrating its superior catalytic kinetics. Long-term electrochemical durability was investigated by subjecting TPE-SAL-Ni CMP700 to 2000 continuous CV cycles. The LSV curves before and after cycling remained nearly identical [Fig. 5(f)], confirming excellent structural stability and catalyst robustness under alkaline OER conditions. The superior electrocatalytic performance of TPE-SAL-Ni CMP700 can be attributed to the synergistic

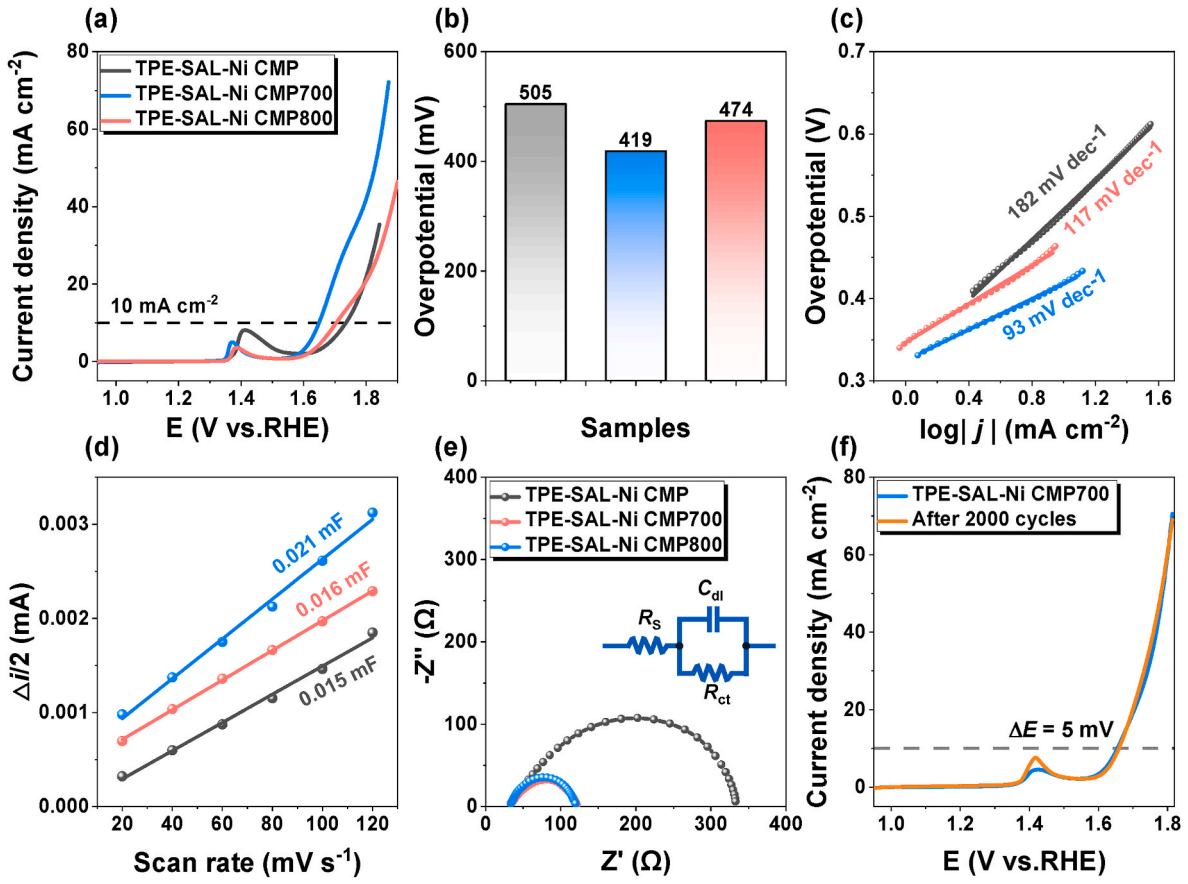

Fig. 5. (a) OER LSV curves, (b) comparison of overpotentials at 10 mA cm^{-2}, (c) Tafel plots, (d) $\Delta i/2$ versus scan rate for C_{dl} evaluation, (e) Nyquist plots of TPE-SAL-Ni CMP, TPE-SAL-Ni CMP700, and TPE-SAL-Ni CMP800, and (f) LSV curves of TPE-SAL-Ni CMP700 before and after 2000 CV cycles.

contributions from uniformly dispersed Ni^0 nanoparticles, residual Ni–N coordination sites, and the nitrogen-doped, graphitized carbon framework. The coexistence of Ni^0 and Ni^{2+}–N species likely facilitates both charge transfer and the stabilization of reaction intermediates, collectively enhancing the intrinsic activity. In addition, the hierarchical tubular architecture promotes electrolyte penetration, while the improved conductivity ensures efficient charge transport. These structural and compositional features work in concert to boost the overall catalytic activity and durability during alkaline OER. To further evaluate the electrochemical durability, the stability of TPE-SAL-Ni CMP700 and TPE-SAL-Ni CMP800 was investigated by chronoamperometric (CA) measurements at a constant potential of 1.64 V (vs. RHE) in 1.0 M KOH. As shown in Fig. S11, TPE-SAL-Ni CMP700 exhibits excellent stability, retaining 99.43% of its initial current density after 16 h of continuous OER operation. In comparison, TPE-SAL-Ni CMP800 shows a slightly lower retention of 96.29% under the same conditions. These results demonstrate the superior long-term catalytic stability and robustness of TPE-SAL-Ni CMP700 in alkaline OER. Post-stability XPS analysis was conducted to probe the chemical stability structures of TPE-SAL-Ni CMP700 and TPE-SAL-Ni CMP800 after 2000 cycles. A new F 1s signal at ~689 eV is observed [Fig. S12], which originates from the Nafion binder [67]. The high-resolution C 1s spectra [Fig. S13(a)] can be deconvoluted into multiple components, including peaks at 284.2-284.3 eV (**C**–C, **C**C, and **C** ≡C), 284.8-284.9 eV (**C**–N, **C**N), and 286.1-286.2 eV (**C**–O). Additional peaks at 289.0-289.2 eV (**C**–SO_3) and 291.4-295.5 eV (**C**–F, **C**–F_2, and **C**–F_3) are attributed to Nafion binder [67]. The N 1s spectra [Fig. S13(b)] display two main contributions: one in the range of 397.0-398.7 eV corresponding to pyridinic-**N**, Pyrrolic-**N** and Ni–**N** coordination, and another at 400.3-400.6 eV assigned to graphitic, quaternary, and oxidized nitrogen species, indicating an increased proportion of graphitic and oxidized nitrogen after OER operation. The O 1s spectra [Fig. S13(c)] show peaks at 530.9-531.0 eV, attributed to C–**O**, N–**O**, or N**O** groups, and at 532.2-532.3 eV corresponding to Ni–**O** coordination, along with an additional component at 534.9-535.1 eV associated with C–S**O**$_3$ species from Nafion binder [68–70]. Notably, the high-resolution Ni $2p_{3/2}$ spectra reveal significant chemical transformation after OER operation [Fig. S14(a)]. New peaks appearing at ~855.7-855.9 eV, 859.8-860.8 eV, and 861.5-861.8 eV are assigned to **Ni**–O, **Ni**$(OH)_2$, and **Ni**OOH species, respectively, indicating the formation of electrochemically active nickel oxyhydroxide phases during OER. Meanwhile, metallic Ni signals are still observed at 851.2-851.7 eV (Ni^0 $2p_{3/2}$) and ~865.0-865.3 eV (Ni^0 $2p_{1/2}$), suggesting the coexistence of metallic and oxidized nickel species. This dynamic transformation from Ni^0/Ni^{2+} to NiOOH under operating conditions provides direct evidence of the active phase evolution and further supports the excellent catalytic performance and stability of the material. Moreover, SEM images of TPE-SAL-Ni CMP700 and TPE-SAL-Ni CMP800 after 2000 cycles are shown in Figs. S14(b)–S14(e). Owing to the presence of carbon black and Nafion binder, both samples display a cauliflower-like porous morphology. Importantly, the metallic Ni nanoparticles remain clearly visible on the catalyst surface, indicating that the overall structural framework is well preserved during prolonged OER operation. In addition, HRTEM images of TPE–SAL-Ni CMP700 [Fig. S15(a) and S15(b)] show that the Ni nanoparticles are still anchored on the surfaces of the hollow carbon tubes, confirming their intimate interfacial contact with the carbon matrix. This robust architecture is expected to facilitate efficient electron transport and maintain high accessibility of the active sites during electrocatalysis. Furthermore, TEM-EDX elemental mapping of TPE-SAL-Ni CMP700 after 2000 cycles [Figs. S15(c)–S15(h)] reveals a homogeneous distribution of C, N,

O, Ni, and F throughout the framework, further demonstrating the structural integrity and compositional stability of the catalyst after long-term operation. Table S4 provides a comprehensive benchmarking of OER performance metrics for the prepared materials [TPE-SAL-Ni CMP, TPE-SAL-Ni CMP700, and TPE-SAL-Ni CMP800] against representative porous organic polymers (POPs) and inorganic electrocatalysts reported in alkaline electrolytes. The outstanding OER performance of TPE-SAL-Ni CMP700 is mainly attributed to its nitrogen-rich framework. The electron-withdrawing nature of nitrogen induces a positive charge on neighboring carbon atoms, which enhances OH^- adsorption and accumulation on the catalyst surface. These positively charged sites facilitate the recombination of adsorbed intermediates in the rate-determining step. In addition, the electron density localized on nitrogen atoms near the Fermi level enables efficient electron transfer, further boosting the electrocatalytic activity [71,72].

4. Conclusions

In this study, we have developed a robust and modular strategy for engineering high-performance oxygen evolution electrocatalysts by thermally transforming TPE-SAL-Ni CMP into Ni/N co-doped hollow carbon microtubes. The coordination of Ni^{2+} with salen-type OPDI ligands facilitated the uniform dispersion of active centers within the CMP framework. At the same time, subsequent carbonization at optimized temperatures enabled the formation of a graphitized, conductive carbon architecture embedded with metallic Ni nanoparticles. Among the synthesized materials, TPE-SAL-Ni CMP700 exhibited the most outstanding OER performance in alkaline media, delivering a low overpotential of 419 mV at 10 mA cm^{-2}, and a favorable Tafel slope of 93 mV dec^{-1}. The coexistence of Ni^0 and Ni^{2+}-N species, confirmed by XPS and TEM analyses, synergistically contributed to the catalytic activity by enhancing charge transport and stabilizing reaction intermediates. Despite a decrease in surface area after pyrolysis, TPE-SAL-Ni CMP700 maintained a hierarchical tubular morphology, efficient electrolyte diffusion pathways, and superior electrochemical surface area, as indicated by C_{dl} and ECSA measurements. This work highlights the structure–property relationship between the local coordination environment, carbonization-induced nanostructure transformation, and electrocatalytic performance. The metal-templated CMP approach, combined with rational pyrolysis, offers a generalizable platform for fabricating earth-abundant, durable, and efficient electrocatalysts. These findings expand the design toolbox for advanced OER catalysts and reinforce the potential of salen-based CMPs as versatile precursors for next-generation energy materials.

CRediT authorship contribution statement

Yang-Chin Kao: Writing – original draft, Formal analysis, Conceptualization, Investigation. **Mohamed Gamal Mohamed:** Writing – review & editing, Writing – original draft, Methodology, Investigation, Formal analysis, Data curation, Conceptualization, Supervision. **Wei-Hsuan Chang:** Data curation, Conceptualization. **Ahmed F. Saber:** Data curation, Conceptualization. **Shiao-Wei Kuo:** Supervision, Project administration, Resources.

Declaration of competing interest

The authors declare that they have no known competing financial interests or personal relationships that could have appeared to influence the work reported in this paper.

Acknowledgments

This study was supported financially by the National Science and Technology Council, Taiwan, under contracts NSTC 113-2223-E-110-001- and 113-2221-E-110-012-MY3. The authors thank the staff at National Sun Yat-sen University for their assistance with the TEM (ID: EM022600)experiments.

Appendix A. Supplementary data

Supplementary data to this article can be found online at https://doi.org/10.1016/j.ijhydene.2026.155356.

Data availability

Data will be made available on request.

References

[1] Li J. Oxygen evolution reaction in energy conversion and storage: design strategies under and beyond the energy scaling relationship. Nano-Micro Lett 2022;14:112. https://doi.org/10.1007/s40820-022-00857-x.
[2] Tahir M, Pan L, Idrees F, Zhang X, Wang L, Zou JJ, Wang ZL. Electrocatalytic oxygen evolution reaction for energy conversion and storage: a comprehensive review. Nano Energy 2017;37:136–57. https://doi.org/10.1016/j.nanoen.2017.05.022.
[3] Rong C, Huang X, Arandiyan H, Shao Z, Wang Y, Chen Y. Advances in oxygen evolution reaction electrocatalysts via direct oxygen–oxygen radical coupling pathway. Adv Mater 2025;37:2416362. https://doi.org/10.1002/adma.202416362.
[4] Zhao Y, Saseendran DPA, Huang C, Triana CA, Marks WR, Chen H, Zhao H, Patzke GR. Oxygen evolution/reduction reaction catalysts: from in situ monitoring and reaction mechanisms to rational design. Chem Rev 2023;123:6257–358. https://doi.org/10.1021/acs.chemrev.2c00515.
[5] Feng Z, Dai C, Shi P, Lei X, Guo R, Wang B, Liu X, You J. Seven mechanisms of oxygen evolution reaction proposed recently: a mini review. Chem Eng J 2024;485:149992. https://doi.org/10.1016/j.cej.2024.149992.
[6] Ying J, Chen JB, Xiao YX, de Torresi SIC, Ozoemena KI, Yang XY. Recent advances in Ru-based electrocatalysts for oxygen evolution reaction. J Mater Chem A 2023;11:1634–50. https://doi.org/10.1039/D2TA07196G.
[7] Song J, Wei C, Huang ZF, Liu C, Zeng L, Wang X, Xu ZJ. A review on fundamentals for designing oxygen evolution electrocatalysts. Chem Soc Rev 2020;49:2196–214. https://doi.org/10.1039/C9CS00607A.
[8] Qin R, Chen G, Feng X, Weng J, Han Y. Ru/Ir-based electrocatalysts for oxygen evolution reaction in acidic conditions: from mechanisms, optimizations to challenges. Adv Sci 2024;11:2309364. https://doi.org/10.1002/advs.202309364.
[9] Thao NTT, Jang JU, Nayak AK, Han H. Current trends of iridium-based catalysts for oxygen evolution reaction in acidic water electrolysis. Small Sci 2024;4:2300109. https://doi.org/10.1002/smsc.202300109.
[10] Angeles-Olvera Z, Crespo-Yapur A, Rodríguez O, Cholula-Díaz JL, Martínez LM, Videa M. Nickel-based electrocatalysts for water electrolysis. Energies 2022;15:1609. https://doi.org/10.3390/en15051609.
[11] Ehsan MA, Ullah Z, Nazar MF, Younas M, Suliman M. One step fabrication of nanostructured nickel thin films on porous nickel foam for drastic electrocatalytic oxygen evolution. Int J Hydrogen Energy 2023;48:15784–95. https://doi.org/10.1016/j.ijhydene.2023.01.083.
[12] Peng W, Li F, Kong S, Guo C, Wu H, Wang J, Shen Y, Meng X, Zhang M. Recent advances in nickel-based catalysts in eCO_2RR for carbon neutrality. Carbon Energy 2024;6:e498. https://doi.org/10.1002/cey2.498.
[13] Huo L, Jin C, Jiang K, Bao Q, Hu Z, Chu J. Applications of nickel-based electrocatalysts for hydrogen evolution reaction. Adv Energy Sustain Res 2022;3:2100189. https://doi.org/10.1002/aesr.202100189.
[14] Salmanion M, Najafpour MM. Oxygen-evolution reaction performance of nickel (hydr) oxide in alkaline media: iron and nickel impurities. J Phys Chem C 2023;127:18340–9. https://doi.org/10.1021/acs.jpcc.3c05164.
[15] Görlin M, Halldin Stenlid J, Koroidov S, Wang HY, Börner M, Shipilin M, Kalinko A, Murzin V, Safonova OV, Nachtegaal M, Uheida A, Dutta J, Bauer M, Nilsson A, Morales OD. Key activity descriptors of nickel-iron oxygen evolution electrocatalysts in the presence of alkali metal cations. Nat Commun 2020;11:6181. https://doi.org/10.1038/s41467-020-19729-2.
[16] Bao F, Kemppainen E, Dorbandt I, Xi F, Bors R, Maticiuc N, Wenisch R, Bagacki R, Schary C, Michalczik U, Bogdanoff P, Lauermann I, Krol RVD, Schlatmann R, Calnan S. Host, suppressor, and promoter—the roles of Ni and Fe on oxygen evolution reaction activity and stability of NiFe alloy thin films in alkaline media. ACS Catal 2021;11:10537–52. https://doi.org/10.1021/acscatal.1c01190.
[17] Hales N, Schmidt TJ, Fabbri E. Reversible and irreversible transformations of Ni-based electrocatalysts during the oxygen evolution reaction. Curr Opin Electrochem 2023;38:101231. https://doi.org/10.1016/j.coelec.2023.101231.
[18] Jo S, Kang B, An S, Jung HB, Kwon J, Oh H, Lim J, Choi P, Oh J, Cho KY, Cho HS, Kim M, Lee JH, Eom K, Fuller TF. High-performance nickel–bismuth oxide electrocatalysts applicable to both the HER and OER in alkaline water electrolysis. ACS Appl Mater Interfaces 2025;17:11946–55. https://doi.org/10.1021/acsami.4c15514.
[19] Hales N, Huang J, Sjølin BH, Garcia-Padilla A, Borca CN, Huthwelker T, Castelli IE, Skoupy R, Clark AH, Andrzejewski M, Andrzejewski N, Casati N, Schmidt TJ, Fabbri E. Confining surface oxygen redox in double perovskites for enhanced

oxygen evolution reaction activity and stability. Adv Energy Mater 2025:2404560. https://doi.org/10.1002/aenm.202404560.
[20] Wang X, Liu B, Duan R, Zhang H, Zhou X, Hu W, Li C. Tailoring the electronic and hydrophilic properties of nickel oxide hydroxides by bismuth incorporation toward enhanced alkaline electrocatalytic water oxidation. Small 2025;21:2411577. https://doi.org/10.1002/smll.202411577.
[21] Wei J, Shao Y, Xu J, Yin F, Li Z, Qian H, Wei Y, Chang L, Han Y, Li J, Gan L. Sequential oxygen evolution and decoupled water splitting via electrochemical redox reaction of nickel hydroxides. Nat Commun 2024;15:9012. https://doi.org/10.1038/s41467-024-53310-5.
[22] Akbari N, Najafpour MM. Decoding natural strategy: oxygen-evolution reaction on the surface of nickel oxyhydroxide at extremely low overpotential. Inorg Chem 2023;62:19107–14. https://doi.org/10.1021/acs.inorgchem.3c03304.
[23] Huang H, Huang J, Zhong G, Xu S, Chen H, Fu X, Kang S, Tu J, Tuo Y, Liao W, Fang B. Carbon-encapsulated Ni nanoparticles catalysts derived from Ni-hexamine coordination frameworks for oxygen reduction reaction and oxygen evolution reaction. Catalysts 2025;15:338. https://doi.org/10.3390/catal15040338.
[24] Ha J, Kim M, Kim YT, Choi J. $Ni_{0.67}Fe_{0.33}$ hydroxide incorporated with oxalate for highly efficient oxygen evolution reaction. ACS Appl Mater Interfaces 2021;13:42870–9. https://doi.org/10.1021/acsami.1c12155.
[25] Khateri M, Najafpour MM. Oxygen-evolution reaction on nickel oxyhydroxide's surface: toward a super catalyst for oxygen-evolution reaction with ultralow overpotentials. ACS Appl Energy Mater 2024;7:5028–37. https://doi.org/10.1021/acsaem.4c00888.
[26] Merida J, Colomer MT, Rubio F, Mazo MA. Highly porous carbon materials derived from silicon oxycarbides and effect of the pyrolysis temperature on their electrochemical response. Int J Mol Sci 2023;24:13868. https://doi.org/10.3390/ijms241813868.
[27] Wang Y, Wang M, Wang Z, Wang S, Fu J. Tunable-quaternary (N, S, O, P)-doped porous carbon microspheres with ultramicropores for CO_2 capture. Appl Surf Sci 2020;507:145130. https://doi.org/10.1016/j.apsusc.2019.145130.
[28] Yu S, Wang L, Li Q, Zhang Y, Zhou H. Sustainable carbon materials from the pyrolysis of lignocellulosic biomass. Mater Today Sustain 2022;19:100209. https://doi.org/10.1016/j.mtsust.2022.100209.
[29] Ding R, Zhou YP, Zhang YC, Chen H, Zeng FR, Wang YT, Liu BW, Wang YZ, Zhao HB. Air-pyrolysis precision synthesis of functional porous carbon materials. Adv Funct Mater 2025;35:2415006. https://doi.org/10.1002/adfm.202415006.
[30] Suresh A, Campos M, Xie K, Makris E, Lovejoy J, Shamsy ME, Liu C, Rowan SJ. Designing thermally compatible template-coating pairs toward dimensionally stable 3D porous carbons with tunable density. Adv Funct Mater 2025:e15814. https://doi.org/10.1002/adfm.202515814.
[31] Liu M, Shi W, Liu H, Guo Y, Yang B, Chang B. Dynamic tailoring porosity and surface chemistry of ultramicroporous carbon spheres for highly selective post-combustion CO_2 capture. ACS Mater Au 2025;5:397–408. https://doi.org/10.1021/acsmaterialsau.4c00168.
[32] Wang T, Lei J, Wang Y, Pang L, Pan F, Chen KJ, Wang H. Approaches to enhancing electrical conductivity of pristine metal–organic frameworks for supercapacitor applications. Small 2022;18:2203307. https://doi.org/10.1002/smll.202203307.
[33] Ma H, Chen Y, Li X, Li B. Advanced applications and challenges of electropolymerized conjugated microporous polymer films. Adv Funct Mater 2021;31:2101861. https://doi.org/10.1002/adfm.202101861.
[34] Zhang B, Wang W, Liang L, Xu Z, Li X, Qiao S. Prevailing conjugated porous polymers for electrochemical energy storage and conversion: lithium-ion batteries, supercapacitors and water-splitting. Coord Chem Rev 2021;436:213782. https://doi.org/10.1016/j.ccr.2021.213782.
[35] Mondal T, Mohamed MG, Mohamed AAK, Kuo SW. Construction of metal-coordinated bipyridine-based conjugated microporous polymers as robust electrocatalysts for hydrogen evolution. ACS Appl Energy Mater 2025;8:7703–13. https://doi.org/10.1021/acsaem.5c00992.
[36] Hayat A, Sohail M, El Jery A, Al-Zaydi KM, Raza S, Ali H, Al-Hadeethi Y, Taha T, Din IU, Khan MA, Amin MA, Ghasali E, Orooji Y, Ajmal Z, Ansari MZ. Recent advances in ground-breaking conjugated microporous polymers-based materials, their synthesis, modification and potential applications. Mater Today 2023;64:180–208. https://doi.org/10.1016/j.mattod.2023.02.025.
[37] Zhou D, Zhang K, Zou S, Li X, Ma H. Conjugated microporous polymers: their synthesis and potential applications in flexible electrodes. J Mater Chem A 2024;12:17021–53. https://doi.org/10.1039/D4TA02085E.
[38] Luo S, Zeng Z, Wang H, Xiong W, Song B, Zhou C, Duan A, Tan X, He Q, Zeng G, Liu Z, Xiao R. Recent progress in conjugated microporous polymers for clean energy: synthesis, modification, computer simulations, and applications. Prog Polym Sci 2021;115:101374. https://doi.org/10.1016/j.progpolymsci.2021.101374.
[39] Xu Y, Jin S, Xu H, Nagai A, Jiang D. Conjugated microporous polymers: design, synthesis and application. Chem Soc Rev 2013;42:8012–31. https://doi.org/10.1039/C3CS60160A.
[40] Mohamed MG, Chen CC, Ibrahim M, Mousa AO, Elsayed MH, Ye Y, Kuo SW. Tetraphenylanthraquinone and dihydroxybenzene-tethered conjugated microporous polymer for enhanced CO_2 uptake and supercapacitive energy storage. JACS Au 2024;4:3593–605. https://doi.org/10.1021/jacsau.4c00537.
[41] Zhao Z, Wang B, You Z, Zhang Q, Song W, Long X. Heterocyclic modulated electronic states of alkynyl-containing conjugated microporous polymers for efficient oxygen reduction. Small 2023;19:2207298. https://doi.org/10.1002/smll.202207298.
[42] Mondal T, Mohamed MG, Puthiyaparambath MF, Thapa R, Kuo SW. Synergistic transition-metal coordination within pyrene- and phenanthroline-tethered conjugated microporous polymers for boosting hydrogen evolution reaction in alkaline media. ACS Appl Energy Mater 2026;9:1790–802. https://doi.org/10.1021/acsaem.5c03684.
[43] Li Y, Wu L, Wang K, Zhou B, Li Q, Li Z, Yan B, Gong C, Wang Q, Jia J, Shen HM, Deng S, Zhang W, She Y. Nitrogen-rich conjugated microporous polymers with improved cobalt (II) density for highly efficient electrocatalytic oxygen evolution. ACS Appl Mater Interfaces 2024;16:8903–12. https://doi.org/10.1021/acsami.3c18620.
[44] Amin K, Ashraf N, Mao L, Faul CF, Wei Z. Conjugated microporous polymers for energy storage: recent progress and challenges. Nano Energy 2021;85:105958. https://doi.org/10.1016/j.nanoen.2021.105958.
[45] He W, Duan J, Liu H, Qian C, Zhu M, Zhang W, Liao Y. Conjugated microporous polymers for advanced chemical sensing applications. Prog Polym Sci 2024;148:101770. https://doi.org/10.1016/j.progpolymsci.2023.101770.
[46] Sun H, Zhou P, Ye X, Wang J, Tian Z, Zhu Z, Ma C, Liang W, Li A. Nitrogen-doping hollow carbon nanospheres derived from conjugated microporous polymers toward oxygen reduction reaction. J Colloid Interface Sci 2022;617:11–9. https://doi.org/10.1016/j.jcis.2022.02.136.
[47] Sun H, Wang J, Li M, Jiao R, Zhu Z, Li A. Rational design of Fe, N co-doped porous carbon derived from conjugated microporous polymer as an electrocatalytic platform for oxygen reduction reaction. J Colloid Interface Sci 2024;673:354–64. https://doi.org/10.1016/j.jcis.2024.06.068.
[48] Yuan K, Hu T, Xu Y, Graf R, Shi L, Forster M, Pichler T, Riedl T, Chen Y, Scherf U. Nitrogen-doped porous carbon/graphene nanosheets derived from two-dimensional conjugated microporous polymer sandwiches with promising capacitive performance. Mater Chem Front 2017;1:278–85. https://doi.org/10.1039/C6QM00012F.
[49] Herrera LAA, Romero DH, Navarro JAC, Ligonio ÁR, Monteon AL, Villanueva JMR, Morales DM, Peralta RC. Transition metal complexes with tetradentate schiff bases (N_2O_2) obtained from salicylaldehyde: a review of their possible anticancer properties. Coord Chem Rev 2024;505:215698. https://doi.org/10.1016/j.ccr.2024.215698.
[50] Akine S, Nabeshima T. Cyclic and acyclic oligo (N_2O_2) ligands for cooperative multi-metal complexation. Dalton Trans 2009:10395–408. https://doi.org/10.1039/b910989g.
[51] Kao YC, Mondal T, Chang WH, Mohamed MG, Kuo SW. Structural tailoring of metal-coordinated salen-tetraphenylethene-based conjugated microporous polymers for superior active alkaline oxygen evolution electrocatalysis. Int J Hydrogen Energy 2025;173:151390. https://doi.org/10.1016/j.ijhydene.2025.151390.
[52] Mohamed MG, Chen TC, Kuo SW. Solid-state chemical transformations to enhance gas capture in benzoxazine-linked conjugated microporous polymers. Macromolecules 2021;54:5866–77. https://doi.org/10.1021/acs.macromol.1c00736.
[53] Mohamed MG, Chang WC, Kuo SW. Crown ether-and benzoxazine-linked porous organic polymers displaying enhanced metal ion and CO_2 capture through solid-state chemical transformation. Macromolecules 2022;55:7879–92. https://doi.org/10.1021/acs.macromol.2c01216.
[54] Weng TH, Mohamed MG, Sharma SU, Mekhemer IMA, Chou HH, Kuo SW. Rationally engineered ultrastable three-dimensional conjugated microporous polymers containing triptycene, tetraphenylethene, and benzothiadiazole units as exceptional high-performance organic electrodes for supercapacitors. ACS Appl Energy Mater 2023;6:9012–24. https://doi.org/10.1021/acsaem.3c01933.
[55] Mohamed MG, Chen CC, Kuo SW. Nitrogen and sulfur co-doped microporous carbon through benzo[c]-1,2,5-thiadiazole-functionalized benzoxazine-linkage porous organic polymer in CO_2 capture and energy storage. React Funct Polym 2025;214:106286. https://doi.org/10.1016/j.reactfunctpolym.2025.106286.
[56] Mohamed MG, Su BX, Kuo SW. Robust nitrogen-doped microporous carbon via crown ether-functionalized benzoxazine-linked porous organic polymers for enhanced CO_2 adsorption and supercapacitor applications. ACS Appl Mater Interfaces 2024;16:40858–72. https://doi.org/10.1021/acsami.4c05645.
[57] Samy MM, Mohamed MG, Kuo SW. Directly synthesized nitrogen-and-oxygen–doped microporous carbons derived from a bio-derived polybenzoxazine exhibiting high-performance supercapacitance and CO_2 uptake. Eur Polym J 2020;138:109954. https://doi.org/10.1016/j.eurpolymj.2020.109954.
[58] Ejaz M, Mohamed MG, Chen YT, Zhang K, Kuo SW. Porous carbon materials augmented with heteroatoms derived from hyperbranched biobased benzoxazine resins for enhanced CO_2 adsorption and exceptional supercapacitor performance. J Energy Storage 2024;78:110166. https://doi.org/10.1016/j.est.2023.110166.
[59] Goyal V, Bhatt T, Kuttasseri A, Mahata A, Zboril R, Natte K, Jagadeesh RV. A biomass-derived nickel-based nanomaterial as a sustainable and reusable catalyst for hydrogenation of arenes and heteroarenes. RSC Sustain 2025;3:2235–45. https://doi.org/10.1039/D5SU00026B.
[60] Veerakumar P, Chen SM, Madhu R, Veeramani V, Hung CT, Liu SB. Nickel nanoparticle-decorated porous carbons for highly active catalytic reduction of organic dyes and sensitive detection of Hg(II) ions. ACS Appl Mater Interfaces 2015;7:24810–21. https://doi.org/10.1021/acsami.5b07900.
[61] Sahoo Y, He Y, Swihart M, Wang S, Luo H, Furlani E, Prasad PN. An aerosol-mediated magnetic colloid: study of nickel nanoparticles. J Appl Phys 2005;98:054308. https://doi.org/10.1063/1.2033145.
[62] Veeman S, Karuppuchamy S. H_2O_2 assisted hydrothermal and microwave synthesis of CuO–NiO hybrid MWCNT composite electrode materials for supercapacitor applications. Ceram Int 2022;48:26806–17. https://doi.org/10.1016/j.ceramint.2022.05.380.
[63] Chen N, Che S, Liu H, Ta N, Li G, Chen F, Ma G, Yang F, Li Y. In situ growth of self-supporting MOFs-derived Ni_2P on hierarchical doped carbon for efficient overall water splitting. Catalysts 2022;12:1319. https://doi.org/10.3390/catal12111319.

[64] Mijowska E, Dymerska A, Leniec G, Maślana K, Aleksandrzak M, Zairov R, Nazmutdinov R, Chen X. Ni-based compounds in multiwalled graphitic shell for electrocatalytic oxygen evolution reactions. Adv Compos Hybrid Mater 2024;7:172. https://doi.org/10.1007/s42114-024-00981-9.
[65] Liu G, Wang B, Wang L, Wei W, Quan Y, Wang C, Zhu W, Li H, Xia J. MOFs-derived $FeNi_3$ nanoparticles decorated hollow N-doped carbon rod for high-performance oxygen evolution reaction. Green Energy Environ 2022;7:423–31. https://doi.org/10.1016/j.gee.2020.10.007.
[66] Yuan M, Sun Y, Yang Y, Zhang J, Dipazir S, Zhao T, Li S, Xie Y, Zhao H, Liu Z, Zhang G. Boosting oxygen evolution reactivity by modulating electronic structure and honeycomb-like architecture in Ni_2P/N,P-codoped carbon hybrids. Green Energy Environ 2021;6:866–72. https://doi.org/10.1016/j.gee.2020.07.012.
[67] Dzara MJ, Artyushkova K, Foster J, Eskandari H, Chen Y, Mauger SA, Atanassov P, Karan K, Pylypenko S. X-ray photoelectron spectroscopy analysis of nafion-containing samples: pitfalls, protocols, and perceptions of physicochemical properties. J Phys Chem C 2024;128:8467–82. https://doi.org/10.1021/acs.jpcc.4c00872.
[68] Mohamed MG, Ejaz M, Basit A, Kao YC, Mohammed AAK, Kuo SW. Conjugated microporous polymers incorporated redox-active hexaazatrinaphtylene and triphenyltrazine moieties for efficient faradaic supercapacitor energy storage. J Energy Storage 2026;154:121329. https://doi.org/10.1016/j.est.2026.121329.
[69] Mohamed MG, Basit A, Mohammed AAK, Kuo SW. 2,2′-Bithiophene and thieno[3,2-b]thiophene-tethered conjugated microporous polymers as organic electrodes for supercapacitor energy storage. Mater Today Chem 2026;53:103492. https://doi.org/10.1016/j.mtchem.2026.103492.
[70] Farghal AF, Mansoure TH, Mohamed MG, Mohammed AAK, Kuo SW. Effect of carbonyl group position on redox-active anthraquinone-, phenanthrenequinone-, and benzil-linked hexaazatrinaphthalene conjugated microporous polymers for supercapacitor electrodes. Chem Eng J 2026;534:174848. https://doi.org/10.1016/j.cej.2026.174848.
[71] Gopi S, Giribabu K, Kathiresan M. Porous organic polymer-derived carbon composite as a bimodal catalyst for oxygen evolution reaction and nitrophenol reduction. ACS Omega 2018;3:6251–8. https://doi.org/10.1021/acsomega.8b00574.
[72] Zhao Y, Nakamura R, Kamiya K, Nakanishi S, Hashimoto K. Nitrogen-doped carbon nanomaterials as non-metal electrocatalysts for water oxidation. Nat Commun 2013;4:2390. https://doi.org/10.1038/ncomms3390.